Drivers of an Ecologically Relevant Summer North American Dipole

HUSILE BAI, a COURTENAY STRONG, AND BENJAMIN ZUCKERBERG

^a Department of Atmospheric Sciences, University of Utah, Salt Lake City, Utah ^b Department of Forest and Wildfire Ecology, University of Wisconsin–Madison, Madison, Wisconsin

(Manuscript received 15 July 2022, in final form 9 December 2022)

ABSTRACT: The teleconnection mechanisms associated with midlatitude climate dipoles are of high interest because of their potential broad impacts on ecological patterns and processes. A prominent example attracting increasing research interest is a summer (June–August) North American dipole (NAD), which drives continental-scale bird irruptions in the boreal forest (semiperiodic movements of large numbers of individual birds). Here, the NAD is objectively defined as a second principal component of 500-hPa geopotential height and is linked to two mechanisms: 1) Rossby waves associated with Madden–Julian oscillation (MJO) convection and 2) a pan-Pacific stationary Rossby wave triggered by East Asian monsoonal convection. The MJO mechanism relates to anomalously frequent occurrence of MJO phase 1 or 6, which are captured by the leading principal component of daily summer MJO phases (PC_{M1}; accounting for 46% of the phase variance). In "nonuniform" MJO summers, defined as $|PC_{M1}| > 0.5$, anomalously frequent phase 1 triggers positive NAD, and anomalously frequent phase 6 triggers negative NAD, yielding the correlation $r(NAD, PC_{M1}) = 0.55$, p < 0.01. During "uniform" MJO summers, defined as $|PC_{M1}| \le 0.5$, the effect of East Asian precipitation anomalies P_{EA} becomes apparent, and $r(NAD, P_{EA}) = 0.49$, p < 0.01. The impacts of P_{EA} are largely masked during nonuniform MJO summers, meaning this subset of summers lacks a significant correlation between the NAD and P_{EA} . Our interpretation is that uniformly distributed MJO allows monsoonal convection over the midlatitudes to modulate the NAD, whereas tropical convection anomalies associated with anomalously frequent MJO phases 1 and 6 overwhelm the extratropical teleconnection.

KEYWORDS: North America; Rossby waves; Teleconnections; Climate variability; Ecosystem effects

1. Introduction

Climate variability alters the behavior, movement, and population dynamics of multiple species and taxa around the world (Alberto et al. 2013; Davis and Shaw 2001). Changes in temperature and precipitation impact both evolutionary (Savolainen et al. 2007) and ecological processes (Princé and Zuckerberg 2015) and can synchronize variability in species abundance, survival, and reproduction over hundreds of kilometers, a phenomenon known as the Moran effect (Moran 1949). There is growing interdisciplinary interest in understanding how climate variability, and climate dipoles in particular, can synchronize ecological processes at regional scales (through the Moran effect) while concurrently imparting asynchronous changes at continental scales (Zuckerberg et al. 2020): in effect, a climate dipole creating an ecological dipole. Bird migration is one of the most visible ecological processes that is strongly connected to climate variability (Alerstam 1993) and could be responsive to climate dipoles. For example, recent work has shown that boreal bird irruptions (the semiperiodic movement of large numbers of birds outside their normal range; Bock and Lepthien 1976; Sokolov et al. 2002) are associated with a climate teleconnection operating across North America resulting in an east-west ecological dipole of irruption dynamics (Strong et al. 2015). These irruptions are common in many seed-eating boreal birds and are theorized to be an adaptation to changes in food supply associated with the "boom-and-bust" economy of conifer

Corresponding author: Courtenay Strong, court.strong@utah.edu

seed production, which in of itself is strongly associated with continentwide fluctuations in temperature and precipitation (LaMontagne et al. 2020).

A common approach for exploring the ecological role of climate variability is to use existing climate indices, such as El Niño-Southern Oscillation (ENSO) or the North Atlantic Oscillation (NAO), as statistical predictors of the interannual variability in ecological data. However, with the modern collection of ecological data at spatial and temporal resolutions analogous to weather data, the climate-ecological discovery process can be inverted by relying on fluctuations in the ecological observations to uncover ecologically relevant climate teleconnections (Zuckerberg et al. 2020). As an example, the underlying mechanisms of boreal bird irruptions lie in the fluctuations of food availability imposed by variable seed production, known as masting (Koenig and Knops 2001; Visser et al. 2009; Newton 2012). Masting is synchronized over thousands of kilometers and is associated with dipoles in temperature occurring a year or two before the masting event (LaMontagne et al. 2020). Consequently, climate dipoles may entrain boreal bird irruptions indirectly by influencing their food supply. Strong et al. (2015) discovered a correlation between climate dipoles and irruptive movements of pine siskins (Spinus pinus), a boreal bird, based around two major directions of migration (west-east and north-south), uncovering continentwide pushand-pull irruptive movements driven by temperature and precipitation anomalies over multiple time lags. The temperature and precipitation anomalies that trigger these irruptions by modulating masting have been documented, but understanding is limited regarding how Rossby waves and specific teleconnection

DOI: 10.1175/JCLI-D-22-0542.1

mechanisms generate these climate dipoles, hindering our ability to understand how they may change in the future.

Atmospheric Rossby waves can form as part of internal atmospheric variability and can propagate outward from convection and precipitation anomalies occurring in so-called "source regions." Understanding the mechanism and source region of atmospheric waves is essential to understanding ecologically relevant downstream precipitation and temperature anomalies. A portion of the potential tropical source dynamics are tied to interannual sea surface temperature variations associated with the ENSO. The Pacific-North American (PNA) sector features extratropical source regions for Rossby waves, often associated with monsoonal convection during spring or summer. Prominent examples include the "Tokyo-Chicago Express" teleconnection (Lau and Weng 2002) and the "Silk Road" pattern (Enomoto et al. 2003). These modes capture connections between East Asian summer monsoon (EAM) convection and central U.S. summer rainfall, and they link geopotential height anomalies over southern Japan and the East Asian summer jet through atmospheric teleconnections. EAM convection is an important Rossby wave source during summer when the background flow is weak and less well organized (Wang et al. 2001; Lopez et al. 2019), and several studies have identified important roles for the EAM in North American climate variability associated with diabatic heating from its deep convection (Sampe and Xie 2010; Zhu and Li 2016, 2018).

The Madden-Julian oscillation (MJO) consists of eastwardpropagating convection and represents one of the most dominant physical modes of tropical intraseasonal variability (Wheeler and Hendon 2004; Barrett 2019). The extratropical response to MJO can be PNA-like, with a low-frequency variability, and the consistency of this signature depends on the arrangement of Rossby wave sources around the subtropical jet (Tseng et al. 2019). Although the MJO is tracked operationally with daily indices, these patterns cumulatively form the dominate mode of intraseasonal (30-90 days) tropical atmospheric variability (Zhang 2005), meaning the MJO has the potential to influence seasonal-scale extratropical dipoles. On longer time scales, recent analyses of the MJO indicate statistically significant power spectrum peaks at 12-20-yr periods attributed in part to variations in sea surface temperature (Wang et al. 2021). Recent work also shows that century-scale reanalyses can skillfully capture characteristics of the MJO despite being forced by sea surface temperatures with minimal data assimilation (Cui et al. 2020), providing an opportunity to understand long-term variations in this important climate mechanism.

It is likely that teleconnections, such as those emanating from the MJO (Matthews 2000) and ENSO (Sillett et al. 2000), potentially influence seed masting and avian irruption by modulating upper-level Rossby wave propagation and jet stream anomalies. However, few studies have attempted to identify the larger-scale atmospheric patterns associated with the most ecologically relevant climate dipoles, and the origins of these dipoles remain elusive. Here, we investigate the teleconnection mechanisms that drive the summer North American dipole (NAD), which appears to be centrally important to the pine siskin west–east irruption mode uncovered by Strong et al. (2015). Data and

methods are presented in section 2. The atmospheric drivers of bird west-east irruption are shown in section 3. Teleconnection between NAD and the tropical MJO-like convection is presented in section 4, and the analysis of extratropical teleconnection between NAD and convective activity over East Asia is examined in section 5. Discussion and conclusions follow in section 6.

2. Data and methods

This section describes the datasets and analysis procedures used in the study. All datasets described below were detrended prior to any calculations. Statistical significance of correlations and anomalies were evaluated using t tests assuming 1 degree of freedom per year. Variability patterns were analyzed using empirical orthogonal function (EOF) analysis (Hannachi et al. 2007), also known as principal component analysis.

a. Datasets

1) BIRD DATA

The magnitude and periodicity of bird irruptions were identified using observations collected during Project Feeder-Watch (PFW; Bonter and Hochachka 2009). Bird (e.g., pine siskin) counts consist of a 2-day observation period separated by 5 days and begin on the second Saturday in November and run for 21 weeks during the winter. For our purposes, we total the bird counts over that period for each site and year in which the collection period ended (e.g., FeederWatch year 1989 corresponds to November 1988-April 1989). PFW has been collecting data since 1989, and over 25 000 participants regularly enlist annually across the United States (Zuckerberg et al. 2011, 2012). Although this dataset has limitations and quality control challenges inherent in citizen science, we followed the processing steps in Strong et al. (2015) to deemphasize small-scale heterogeneity and minimize artifacts stemming from, for example, oversampling of urban or suburban areas. With this processing, the FeederWatch data are well suited for the project due to their continental extent, large sample size, and repeated sampling throughout the Northern Hemisphere winter when irruptions are most likely to occur. We chose pine siskin as the focal species because they are one of the most visible and widespread North American seed-eating birds, and they also engage in irruptive movements (Watts et al. 2017). Data for 1989-2019 are analyzed here as further detailed below in section 2b.

2) CLIMATE DATA

Reanalysis datasets from 1950 to 2019 for monthly averaged 500-hPa geopotential height Z_{500} , near-surface (2-m) air temperature, and outgoing longwave radiation (OLR) were based on the European Centre for Medium-Range Weather Forecasts (ECMWF) reanalysis (ERA5) on a 30-km grid (Hersbach et al. 2020). The datasets used for multidecadal analyses in section 4 were obtained from NOAA Physical Science Laboratory (PSL)'s Twentieth Century Reanalysis (20CR) version 3 on a 1° grid (Compo et al. 2011). Sea surface temperature data were from the Hadley Centre Sea Ice and Sea Surface Temperature

dataset (HadISST) on a 1° grid (Titchner and Rayner 2014). Two precipitation datasets were used. The PFW bird data overlapped with the satellite era, so correlations between migration and precipitation were assessed using Global Precipitation Climatology Project (GPCP) monthly data on a 2.5° grid from 1979 to 2019, which merged rain gauge stations, satellites, and sounding observations (Huffman et al. 1997). For analyses covering the period extended back before the PFW data, we used Global Precipitation Climatology Centre (GPCC) gauge-based data on a 1° grid from 1950 to 2019 (Schneider et al. 2008).

b. Bird dipole analysis

Bird count observations from PFW were mapped to grids for the period 1989-2019 using inverse square root distance weighting on a grid with 141-km spacing following Strong et al. (2015). FeederWatch leading modes of pine siskin count variability were then determined via EOF analysis. In this application, the set of standardized time series of pine siskin count at n = 1003 sites, each with record length m = 31 years, were assembled into a $(n \times m)$ matrix. The EOFs were the eigenvectors of the associated $(n \times n)$ spatial covariance matrix. Further processing details followed prior work with these data (Strong et al. 2015). For each mode, the EOF analysis yielded a time series index (principal component) and a spatial pattern displayed by mapping the correlation between the mode's principal component and the pine siskin count time series at each grid location. The mode's temporal pattern was displayed by plotting the standardized (z score) principal component versus year, indicating the sign and magnitude of the mode. Here, z score means the time series was transformed to have zero mean and unit standard deviation.

To understand how climate variability influences irruption, we correlated climate fields such as 2-m air temperature with the bird count principal component defined above. For this correlation analysis, the climate data (JJA 1986–2016) led the bird irruption principal component (November–April 1989–2019) three summers prior to account for the lags associated with the tree reproductive cycle and bird migration. This lag was motivated by and consistent with prior work by Strong et al. (2015), where it was referred to as y_{-2} (the summer immediately preceding the FeederWatch period was referred to as y_0).

c. Rossby wave source

We computed the linearized Rossby wave source (RWS; Sardeshmukh and Hoskins 1988)

$$RWS = -\nabla \cdot (\mathbf{u}_{\chi}'\overline{\zeta}_{a}) - \nabla \cdot (\overline{\mathbf{u}}_{\chi}\zeta_{a}'), \tag{1}$$

and the vorticity budget (Kosaka and Nakamura 2006)

RWS
$$-\overline{u}_{\psi} \frac{\partial \zeta'_{a}}{\partial x} - \overline{v}_{\psi} \frac{\partial \zeta'_{a}}{\partial y} - u'_{\psi} \frac{\partial \overline{\zeta}_{a}}{\partial x} - v'_{\psi} \frac{\partial \overline{\zeta}_{a}}{\partial y} - \text{(residuals)}$$

 $- \text{(damping)} = 0,$ (2)

where $\mathbf{u}_{\psi}=(u_{\psi},v_{\psi})$ is the rotational wind, $\mathbf{u}_{\chi}=(u_{\chi},v_{\chi})$ is the divergent wind, and ζ_a is the vertical component of the absolute

vorticity. Overbars indicate climatological averages (the mean over all JJA months from 1950 to 2019), and primes indicate the corresponding JJA anomalies in the subset of summers being analyzed (e.g., summers with anomalously high East Asian precipitation). The use of monthly data for our Rossby wave source analysis is consistent with related studies (e.g., Kosaka and Nakamura 2006) and prior work finding that using daily rather than monthly means had a small impact on the seasonal average source (e.g., Scaife et al. 2017).

The terms in Eq. (2) can be split into mean zonal and meridional advection (MA) of anomalous vorticity $ZA \Leftarrow (-\overline{u}_{\psi}\partial\zeta'_{a}/\partial x)$ and $MA \Leftarrow (-\overline{v}_{\psi}\partial\zeta'_{a}/\partial y)$ and the horizontal advection of the mean absolute vorticity by anomalous winds $\beta \Leftarrow (-u'_{\psi}\partial\overline{\zeta}_{a}/\partial x - v'_{\psi}\partial\overline{\zeta}_{a}/\partial y)$, respectively. The (residuals) term represents the vertical advection, tilting, and nonlinear effects. We computed the fields of vorticity, horizontal divergence, and the rotational and divergent wind components based on the zonal and meridional wind velocities by using a spectral expansion with T42 truncation.

d. Madden-Julian oscillation

Variability associated with the MJO was analyzed in a manner similar to the method used for the real-time multivariate MJO (RMM; Wheeler and Hendon 2004). Specifically, the first two empirical orthogonal functions EOF1 and EOF2 of combined daily OLR, 850-hPa zonal wind u_{850} , and 200-hPa zonal wind u_{200} defined the MJO spatial patterns. Prior to the principal components analysis, these fields were meridionally averaged over the equatorial region (15°S-15°N) at all longitudes, and the annual cycle was removed by subtracting the time mean and first three harmonics at each grid point. The removal of ENSO followed the two-step regression procedure used for the RMM but using a Niño-3.4 index based on HadISST (5°S-5°N, 120°-170°W). While the RMM method removes additional interannual variability, decadal variability, and trends by subtracting the 120-day mean of the previous 120 days, we did not perform this additional high-pass filtering because we are interested in understanding how interannual-to-decadal variability in tropical convection influences the teleconnections of interest in this study. We refer to the EOFs resulting from this procedure as the unfiltered multivariate MJO indices (UMM1 and UMM2). Note that the removal of the annual cycle and ENSO was performed only for the inputs to the UMM calculations, meaning all other data presented in the study have not been filtered.

The UMM patterns were analyzed using 20CR daily data because our interests include the effects of potentially multidecadal variability in tropical convection. 20CR data assimilation is limited to surface pressure reports and uses observed monthly SST and sea ice as boundary conditions. Observations informing 20CR become sparser back in time, but independent radiosonde data indicate that the reanalysis is of generally high quality over the Northern Hemisphere extratropics (Compo et al. 2011). The spatial and temporal patterns of the UMM indices derived from the 20CR compare favorably with the analogous results derived from shorter, satellite-informed reanalyses. The UMM indices had spatial patterns (Figs. 1a,b) very similar

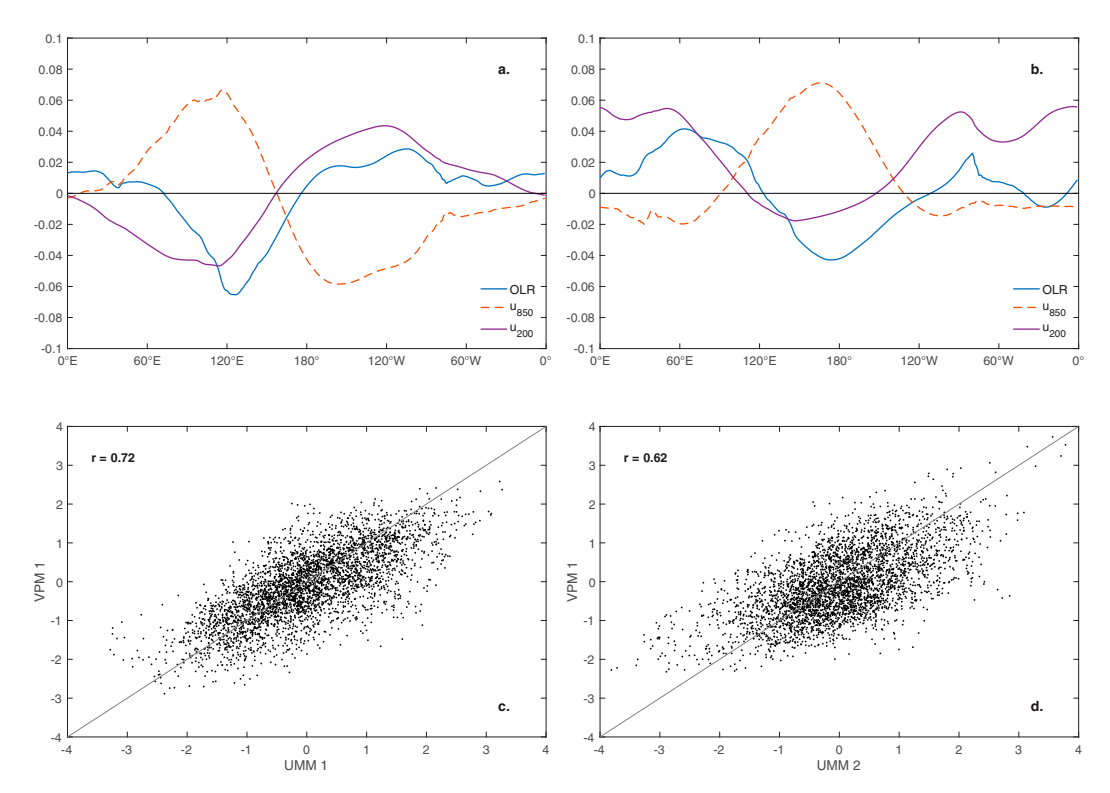


FIG. 1. The leading two EOF_s (a) EOF₁ and (b) EOF₂ from the multivariate EOF analysis using daily OLR, u_{850} , and u_{200} from 20CR (1870–2015) processed as detailed in section 2d. These EOFs were used to produce the corresponding unfiltered multivariate MJO indices UMM1 and UMM2. (c),(d) Comparison of UMM1 and UMM2 to analogous indices VPM1 and VPM2 based on velocity potential MJO obtained from NOAA Physical Sciences Laboratory (Ventrice et al. 2013) for the overlapping period (1979–2019).

to the corresponding EOF patterns used in the real-time multivariate MJO index (Wheeler and Hendon 2004). For example, EOF₁ featured enhanced convection (negative OLR anomalies, blue curves), increased low-level westerly wind (positive u_{850} , dashed red curves), and reduced upperlevel easterly wind (negative u_{200} , purple curves) throughout the east Indian and western Pacific Oceans (Fig. 1a). EOF₁ and EOF₂ explained 18.6% and 14.4% of the variance, respectively (similar to ~12% for RMM), and separated well with the remaining EOFs, which explained 7.8% or less. Also, the UMM indices correlated well $(r \ge 0.62)$ with the velocity potential MJO indices (VPM; Figs. 1c,d), also known as the modified RMM (Ventrice et al. 2013). MJO-related convection typically leads the circulation response by several weeks (Li et al. 2015), and we used the UMM daily values from 1 May through 31 July to lead JJA by 1 month.

3. Atmospheric drivers of west-east irruption mode

The leading mode of variability in pine siskin count for 1989–2019 is a north-south irruption that is highly intermittent, occurring only a few times in the past several decades (Strong et al. 2015). The climate drivers of the north-south mode are being studied as part of ongoing work. Here, we

focus on the second most important mode (EOF₂) of pine siskin count variability, which captures a west-east irruptive migration (Fig. 2a), hereafter referred to as the west-east mode (WEM; Strong et al. 2015), accounting for 12% of the variance. When the west-east mode index (WEM; Fig. 2b) is positive, bird counts are anomalously high over the boreal forest in western North America (red shading, Fig. 2a) and anomalously low over the boreal forest in the eastern boreal forest (blue shading, Fig. 2a). Negative WEM $_i$ corresponds to the reverse pattern. We focus on the boreal forest here but note that the WEM has a quadpole structure with a slightly weaker dipole south of the boreal forest over the continental United States. The WEM, has an interesting temporal pattern with more distinguished biennial fluctuations before 2000, and such changes in periodicity have been noted in other bird migration analyses (Koenig 2001, and references therein). We also note that the three most negative WEM_i years occurred prior to 2000, whereas the three most positive WEM, years are distributed more uniformly through the record.

Correlations with the climate data leading the WEM by 2 years $(y_{-2},$ section 2b) capture a distinct continental-scale west–east dipole of 2-m air temperature and precipitation over the North American boreal forest where climate variability is a plausible driver of irruptions (Figs. 3b,c), indicating cold and wet west and warm and dry east, consistent with prior work (Strong

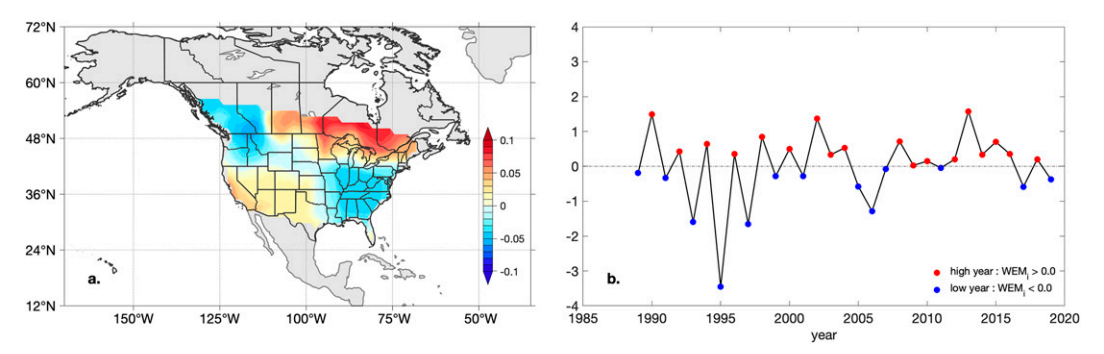


FIG. 2. For pine siskin WEM: (a) loading pattern of the WEM, which is the second principal component of bird counts. (b) WEM_i with red dots indicating positive WEM_i years and blue dots indicating negative WEM_i years. Note that the sign of the WEM_i is reversed from our prior work (Strong et al. 2015) to facilitate understanding how this mode connects to upstream climate dynamics.

et al. 2015). These precipitation and temperature anomaly patterns align logically with the associated Z_{500} pattern (i.e., Z_{500} anomalies match the sign of the underlying temperature anomalies, and conditions are wetter than average downstream from

the Z_{500} trough axis and drier than average downstream from the ridge axis).

The dipole over North America aligns well with the second EOF of JJA Z_{500} in ERA5 (cf. blue contours in Fig. 4d to Fig. 3a).

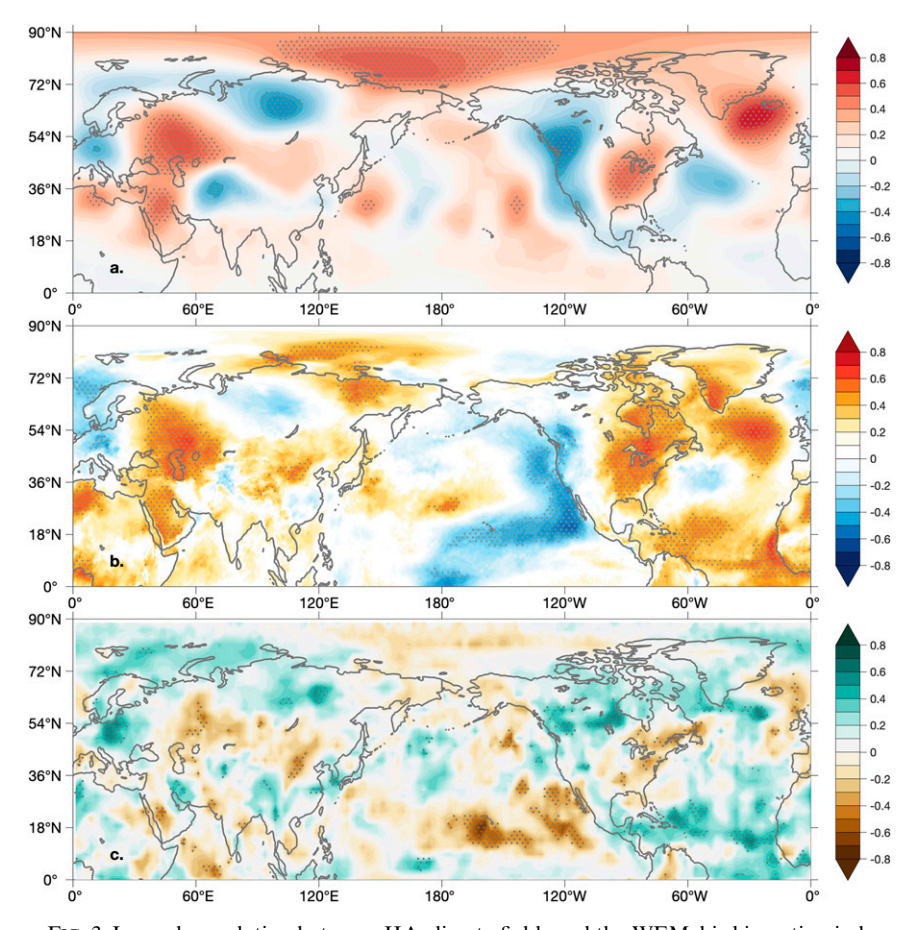


FIG. 3. Lagged correlation between JJA climate fields and the WEM $_i$ bird irruption index: (a) ERA5 500-hPa geopotential height Z_{500} , (b) ERA5 2-m air temperature, and (c) GPCP precipitation. In these correlations, the climate data (1986–2016) led the bird irruption data (1989–2019) to account for the lags associated with the tree reproductive cycle and bird migration. Stippling indicates statistical significance at the 95% confidence level.

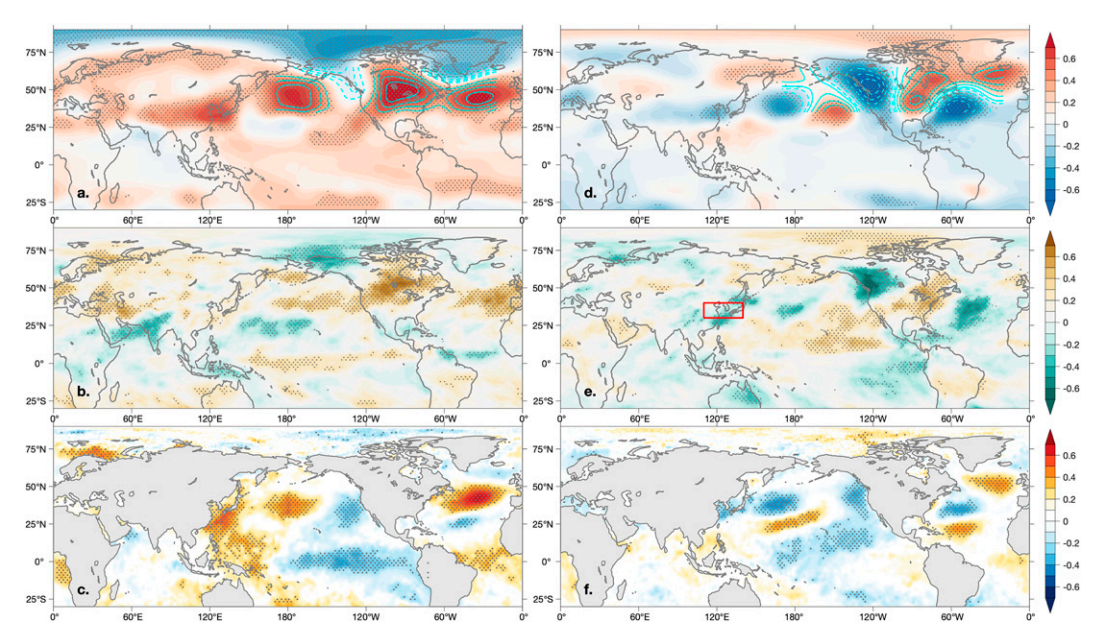


FIG. 4. For the first EOF of JJA Z_{500} in ERA5 over the domain of 35°-65°N, 170°-340°E: (a) loading pattern (blue contours with negative values dashed) and correlation with JJA Z_{500} (shading), (b) correlation with JJAOLR, and (c) correlation with HadISST. (d)-(f) As in (a)-(c), but for the second EOF, which defines the North American dipole index (NAD_i^{ERA5}). Results correspond to 1950-2019, stippling indicates statistical significance at the 95% confidence level, and the red box is the averaging region for the East Asian precipitation index (P_{EA}) defined in section 5.

The associated principal component accounts for 14% of the Z_{500} variance, and we refer to it as the North American dipole index NAD_i^{ERA5}. The NAD_i^{ERA5} is significantly correlated with the WEM_i when it leads it by 2 years (red and blue curves, Fig. 5; r=0.58, p<0.01) and enables us to objectively extend our analysis of this circulation pattern prior to the FeederWatch record. Variance in the WEM_i not accounted for by the NAD_i stems from 1) other weather and climate patterns that

influence masting and 2) population variations in pine siskin not directly tied to atmospheric variability. The NAD resembles the western Pacific–North American (WPNA) teleconnection pattern in its negative polarity, where WPNA tends to occur in summers following peak ENSO phases and is associated with western North Pacific summer monsoon (WNPSM) rainfall anomalies (Ding et al. 2011). As context, we note that the first EOF of JJA Z_{500} accounts for 18.7% of

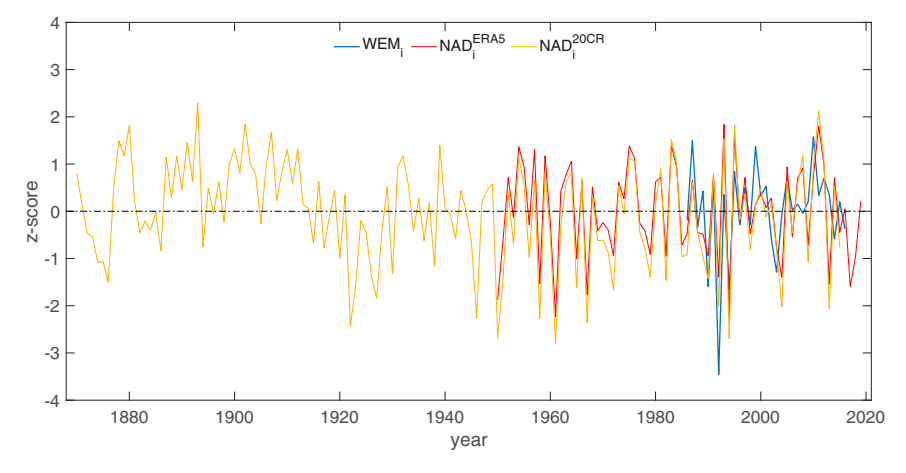


FIG. 5. The WEM index (WEM_i, blue curve), the NAD index defined as a second principal component of Z_{500} in ERA5 (NAD_i^{ERA5}, red curve), and the NAD index derived from 20CR (NAD_i^{20CR}, yellow curve) by projecting 20CR Z_{500} anomalies onto the ERA5 NAD loading pattern (blue contours, Fig. 4d). The WEM_i corresponds to 1989–2019 and is shifted to 1986–2016 to account for the lag between the climate signal and the bird response.

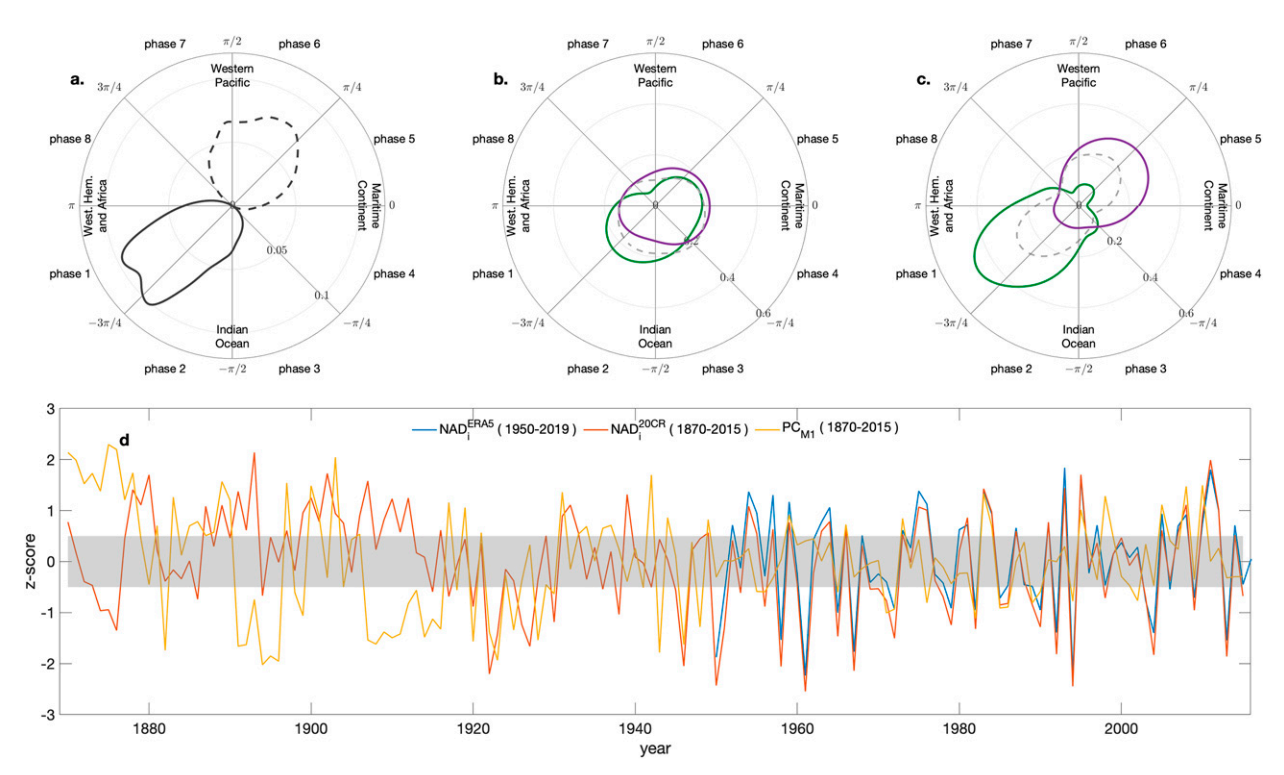


FIG. 6. (a) The loading pattern of the leading principal component of daily UMM phases in 20CR for 1870–2015 (PC_{M1} , negative values dashed). (b) For uniform MJO summers defined as $|PC_{M1}| \le 0.5$, distribution of MJO phases for all values of NAD_i^{ERA5} (dashed gray curve), for NAD_i^{ERA5} above its upper quartile (green curve) and for NAD_i^{ERA5} below its lower quartile (purple curve). (c) As in (b), but for nonuniform MJO summers defined as $|PC_{M1}| > 0.5$. The analysis period in (b) and (c) is 1950–2015 to correspond to overlapping records of ERA5 and 20CR, and the UMM indices lead the JJA NAD analysis period by 30 days, meaning they are for 1 May–1 Aug. (d) Time series of NAD_i^{ERA5} , NAD_i^{20CR} , and PC_{M1} , where the gray shading indicates uniform MJO summers.

the Z_{500} variance and resembles the summer circumglobal teleconnection (CGT) identified by Ding et al. (2011). We use the NAD $_i^{\rm ERA5}$ hereafter as an index of the most important atmospheric circulation pattern associated with the WEM dipole (i.e., the most strongly correlated of the two leading EOFs of geopotential height).

4. Role of Madden-Julian oscillation

Correlation maps of NAD_i^{ERA5} with climate data in Figs. 4d-f suggest that tropical Pacific convection is important to the Rossby wave, which modulates the NAD, and this convection (shading, Fig. 4e) appears to be only weakly tied to tropical SST variability including ENSO (Fig. 4f). We hypothesize that the tropical convection signal thus reflects summerto-summer variations in the relative frequency or intensity of MJO phases. We find that variations in the distribution of MJO phase are most robustly visible when analyzing multiple decades, meaning that MJO-like variability on interannual and longer time scales (Wang et al. 2021; Dasgupta et al. 2021) is an important component of the mechanism. To illustrate this, we produce an extended NAD index by projecting 20CR JJA Z_{500} anomalies onto the NAD loading pattern derived from ERA5 (i.e., blue contours, Fig. 4d) from 1870 to 2015 NAD_i^{20CR} (yellow curve in Fig. 5). This extended NAD_i^{20CR}

index agrees well with NAD_i^{ERA5} for the overlapping period (r = 0.98, p < 0.01; Fig. 5).

The MJO mechanism relates to anomalously frequent occurrence of MJO in phases around either 1 or 6, which is captured by an EOF analysis of daily summer MJO phases. For this EOF analysis, the analyzed data are the eight time series $[f_1, f_2, \dots, f_8]$, where f_n indicates the fraction of summer days assigned to MJO phase n. The leading pattern from this EOF analysis PC_{M1} has the loading pattern shown in Fig. 6a and accounts for 46% of the total variance in daily summer MJO phase. The associated time series is shown by the yellow curve in Fig. 6d. We use the condition $|PC_{M1}| > 0.5$ to define "nonuniform MJO" summers and $|PC_{M1}| < 0.5$ to define "uniform MJO" summers (gray shading, Fig. 6d). Uniform MJO summers lacked a preference for any particular phase (gray dashed curve, Fig. 6b), and positive NAD only slightly favored phases 1 or 2 (green curve, Fig. 6b), while negative NAD slightly favored phases 5 or 6 (purple curve, Fig. 6b). In nonuniform MJO summers, by contrast, the distribution of phases was strongly polarized (gray dashed curve, Fig. 6c), with positive NAD clearly favoring phases around 1 or 2 (green curve, Fig. 6c) and negative NAD favoring phases around 5 or 6 (purple curve, Fig. 6c). Consistent with these relationships, PC_{M1} was significantly correlated with NAD_i^{ERA5} (r = 0.42, p < 0.01) and NAD_i^{20CR} (r = 0.46, p < 0.01) during

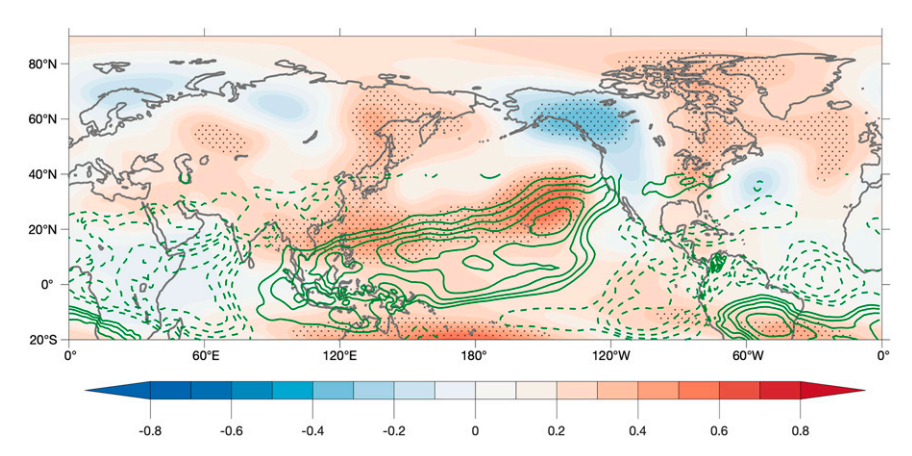


FIG. 7. Correlation maps of PC_{M1} with JJA-mean 20CR Z_{500} (shading) and OLR anomalies (contours; with negative values dashed). The daily UMM values correspond to 1 May–1 Aug to lead the JJA analysis period by 30 days, stippling indicates significance at the 95% confidence level, and the analysis period is 1950–2015.

the overlapping period 1950–2015 (blue, red, and yellow curves, Fig. 6c). The relationship between PC_{M1} and NAD_i^{20CR} lost statistical significance prior to around 1920 (yellow and red curves, Fig. 6d), and this decoupling could reflect a change in the teleconnection mechanism or uncertainty in 20CR stemming from a lower density of assimilated data early in the record.

Correlating ERA5 OLR with PC_{M1} for the overlapping period (1950–2015) reveals negative OLR anomalies indicative of enhanced convection in the western Indian Ocean and eastern tropical Pacific with positive OLR anomalies north of the Maritime Continent (green contours, Fig. 7). The signs resulting from the correlation would correspond to the anomaly signs during phase 1 (because PC_{M1} is positive during anomalously frequent phase 1 per Fig. 6a), and phase 6 would correspond to the reverse signs. The associated extratropical circulation anomalies resemble the positive NAD pattern

with significant ridging northeast of Hawaii, over East Asia, and over eastern North America (shading, Fig. 7). The preceding is evidence of a role for MJO in modulating the NAD, and this mechanism is even more apparent when separating the record into uniform MJO and nonuniform MJO summers defined by shading in Fig. 6d. In nonuniform MJO summers, the NAD is paired with statistically significant upstream ridging northeast of Hawaii and over eastern Russia (Fig. 8b). The nonuniform MJO summer correlation results also feature expansive statistically significant tropical OLR signatures (Fig. 8d) consistent with anomalously frequent MJO around phase 1 triggering positive NAD and anomalously frequent MJO around phase 6 triggering negative NAD. In uniform MJO summers, by contrast, the NAD appears more strongly teleconnected to a pan-Pacific Rossby wave, which traces upstream to significant geopotential height anomalies around Japan (Fig. 8a), and the associated tropical convection patterns are much

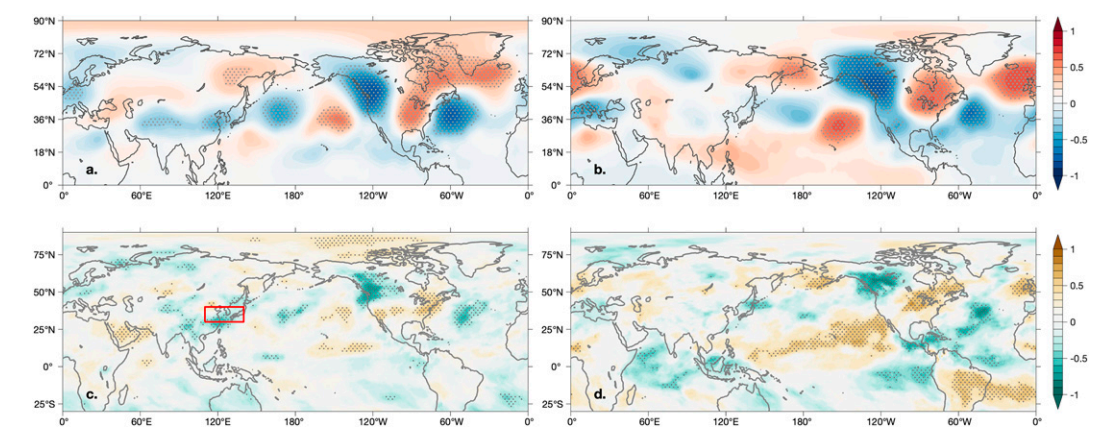


FIG. 8. Correlation of ERA5 Z_{500} with NAD_i^{ERA5} (a) in uniform MJO summers and (b) in nonuniform MJO summers defined by shading in Fig. 6d. (c),(d) As in (a) and (b), but for ERA5 OLR. Stippling indicates statistical significance at the 95% confidence level, the analysis period is the overlap between 20CR and ERA5 (1950–2015), and the red box in (c) is the averaging region for the East Asian precipitation index ($P_{\rm EA}$).

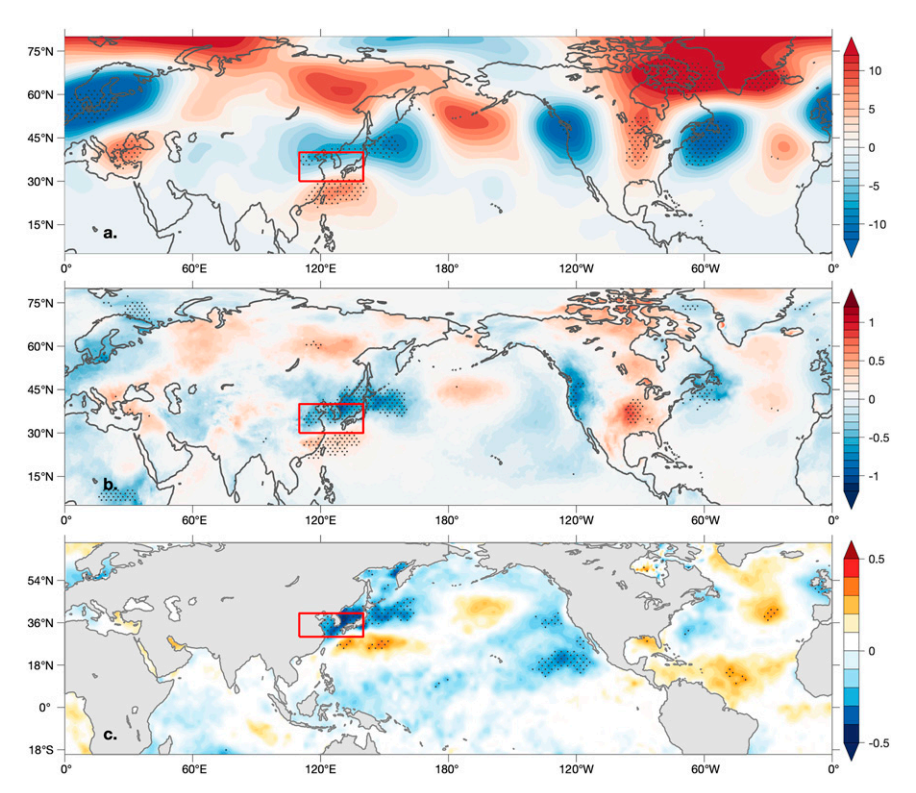


FIG. 9. For high $P_{\rm EA}$ summers (above the 25th percentile), composite mean anomalies of ERA5 (a) Z_{500} (shading; gpm) and (b) 2-m air temperature (shading; °C). (c) Correlation between $P_{\rm EA}$ and JJA-mean sea surface temperatures (HadISST; shading). Stippling indicates statistical significance at the 95% confidence level, the analysis period is 1950–2019, and the red box indicates the averaging region for the $P_{\rm EA}$ index.

weaker (Fig. 8c). These results for uniform MJO summers suggest a role for East Asian monsoonal convection, which is the focus on the next section.

5. Role of East Asian monsoonal convection

Correlation of Z_{500} with NAD_i^{ERA5} features a dipole over the East China Sea and Pacific Japan area (Fig. 4d), indicating an enhanced pressure gradient south of Japan. This potential source region for the pan-Pacific atmospheric wave also corresponds to low OLR (Fig. 4e), indicating increased convective activity near Japan, which resembles the WPNA pattern (Ding et al. 2011) in its negative polarity. Further, SST correlation with NAD_i^{ERA5} shows a significant tripole pattern over the central Pacific (Fig. 4f), which closely resembles the SST pattern that Wang et al. (2001) found in comparing strong and weak instances of the WNPSM (their Fig. 9b).

To explore the role of East Asian monsoonal convection in the NAD further, we introduce a precipitation East Asia $P_{\rm EA}$ index, defined as the area-mean JJA GPCC precipitation over the red box in Fig. 9. Circulation, convection, and precipitation in this region are closely tied to the western North Pacific summer monsoon (Wang et al. 2001), and $P_{\rm EA}$ and NAD $_i^{\rm ERAS}$ are positively correlated (r=0.33, p<0.01). The connection between the NAD and $P_{\rm EA}$ is stronger for uniform MJO summers

 $[r({\rm NAD}_i^{\rm ERAS}, P_{\rm EA})=0.49,\ p<0.01]$ and lacks significance for nonuniform MJO summers $[r({\rm NAD}_i^{\rm ERAS}, P_{\rm EA})=0.09,\ p<0.66]$. This contrast in correlation supports the interpretation that uniformly distributed MJO allows monsoonal convection over the midlatitudes to modulate the NAD, whereas tropical convection anomalies associated with anomalously frequent MJO phases 1 and 6 overwhelm the extratropical teleconnection.

Relatively high precipitation over East Asia ($P_{\rm EA}$ above its 75th percentile) is associated with a zonally elongated dipole pattern over the East China Sea and northern Japan region (Figs. 9a,b), which is familiar from prior work (Wang et al. 2001; Lau and Weng 2002). A pan-Pacific Rossby wave pattern propagates poleward and eastward from this region, projecting positively onto the NAD (Fig. 9a), similar to results obtained for uniform MJO summers (Fig. 8a). The result also shows that $P_{\rm EA}$ is significantly correlated with SST over southern Japan and the East China Sea area and not significantly correlated with tropical SSTs in JJA (Fig. 9b), suggesting a weak influence of ENSO-like variability on $P_{\rm EA}$.

Providing additional evidence of an important role for East Asian monsoonal convection in the NAD, we present a Rossby wave source analysis for uniform MJO summers with high $P_{\rm EA}$ (Fig. 10). Here, we focus the RWS analysis domain and discussion on the oceanic sector following Kosaka and Nakamura (2010). Over the East China Sea and Japan, we

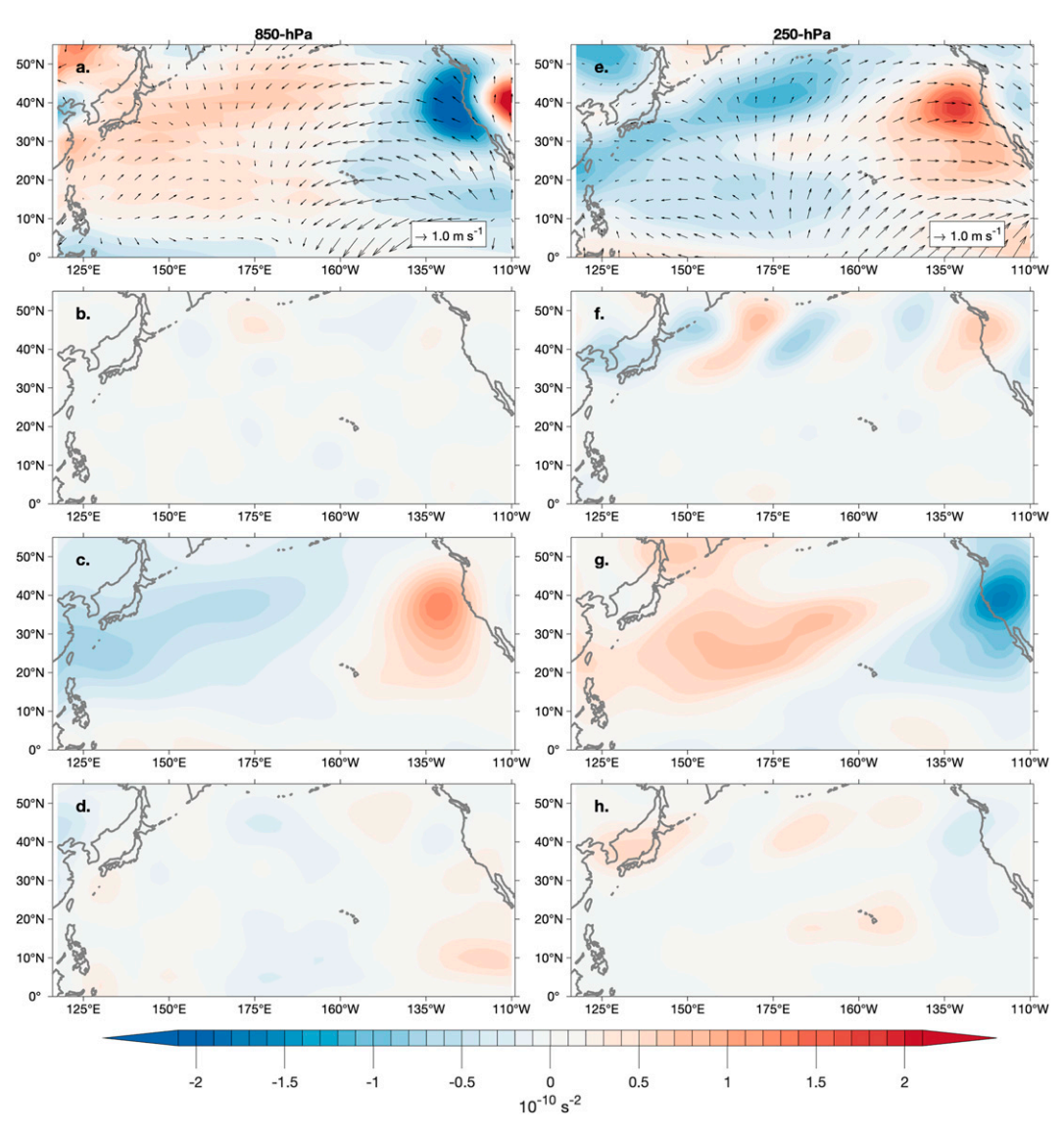


FIG. 10. For uniform MJO summers ($|PC_{M1}| \le 0.5$) with high P_{EA} (above its 75th percentile), 850-hPa (a) Rossby wave source (shading) and irrotational wind (vectors), (b) ZA term, (c) MA term, and (d) β term. (e)–(h) As in (a)–(d), but for 250-hPa. Results correspond to JJA for 1950–2019 based on ERA5 data.

find convergence of the irrotational wind with a positive Rossby wave source in the lower troposphere (red shading, Fig. 10a), corresponding to an increasing tendency of cyclonic vorticity. The overlying pattern in the upper troposphere has divergent irrotational wind and a negative Rossby wave source. This indicates ascending motion between the lower-level convergent and upper-level divergent zone and is consistent with the negative OLR anomaly over East Asia in Fig. 8c. The Rossby wave source is dominated by the vortex stretching term and is compensated mostly by the meridional advection of the anomaly vorticity (Figs. 10c,g). Results indicate that the advection of perturbation vorticity by the mean flow [zonal advection (ZA)] tends to be compensated by the β effect, indicating that the wavy anomalies are largely associated with free Rossby waves (Figs. 10b,f,d,h). We note that there are strong

upstream RWS signals (e.g., over the Mediterranean and Himalayas) that may be related to the NAD teleconnection, but these RWS signals are also robust features of observed and simulated summer RWS climatologies (e.g., Nie et al. 2019; Fuentes-Franco et al. 2022).

6. Discussion and conclusions

Avian irruption is known to be related to summertime near-surface air temperature and precipitation anomalies in the preceding 2–3 years (Zuckerberg et al. 2020). Strong et al. (2015) identified continental-scale irruption patterns of North American boreal seed-eating birds using objective statistical techniques and related these irruptions to climate dipoles. They named these dipoles the north–south irruption mode

and the west-east irruption mode, where the WEM features cold and wet anomalies over western North America and warm and dry anomalies over eastern North America during the boreal summer 2 years before the bird irruptions. In this study, we addressed the following two problems: 1) how do atmospheric circulation and global teleconnections impact avian irruptions at continental scales, specifically the WEM? 2) What summer climate mechanisms generate the Rossby waves ultimately responsible for the ecologically relevant NAD?

The NAD was objectively defined as a second principal component of 500-hPa geopotential height and was linked to two mechanisms: 1) Rossby waves associated with MJO-like convection and 2) a pan-Pacific stationary Rossby wave triggered by EAM convection. The MJO mechanism is linked to anomalously frequent occurrence of either MJO phases 1 or 6, which are captured by the leading principal component of MJO phase based on the daily UMM indices PCM1. In nonuniform MJO summers ($|PC_{M1}| > 0.5$), anomalously frequent phase 1 triggered a poleward- and eastward-propagating Rossby wave conducive to positive NAD, and anomalously frequent phase 6 triggered the reverse. The linkage between MJO phase and the NAD was robust over the full record of ERA5 (1950-2019) and in the 20CR after around 1920, with the correlation breaking down for earlier years. This may indicate a change in the teleconnection mechanism or may just reflect the lower density of assimilated data early in the NOAA 20CR. Despite this change in correlation early in the record, the MJO indices based on NOAA 20CR aligned very well with more modern operational indices (section 2d), and the NAD indices from 20CR and ERA5 were highly correlated (r = 0.98) for the overlapping period 1950-2015.

The second teleconnection mechanism associated with the NAD arises during uniform MJO summers ($|PC_{M1}| \leq 0.5$), when East Asian precipitation anomalies P_{EA} trigger a standing Rossby wave traversing the Pacific from the East China Sea and Japan area eastward across North America, linking high P_{EA} to positive NAD. For uniform MJO summers with high P_{EA} , a Rossby wave source analysis indicated production of cyclonic vorticity in the East China Sea and Japan region, mainly by vortex stretching, which was compensated by meridional advection. Although the Rossby wave source analysis further supports an important role for East Asian convection in the NAD, it is ultimately confounded by simultaneous occurrence of cause and effect in observations, and we have atmospheric boundary forcing experiments underway to explore the underlying causality.

High $P_{\rm EA}$ is in general associated with an elongated dipole tropospheric circulation pattern over southern Japan consistent with prior studies (Nitta 1987; Kosaka and Nakamura 2006, 2010), and this connected to a distinctive downstream pan-Pacific Rossby wave extending across North America to the western Atlantic. The far-reaching impacts of East Asian summer monsoonal precipitation is consistent with prior work highlighting teleconnections between the western North Pacific summer monsoon and North American summer climate (Wang et al. 2001; Ding et al. 2011). The impacts of $P_{\rm EA}$ are largely masked during nonuniform MJO summers, meaning this subset

of summers lacks a significant correlation between the NAD and $P_{\rm EA}$. Our interpretation is that uniformly distributed MJO allows monsoonal convection over the midlatitudes to modulate the NAD, whereas tropical convection anomalies associated with anomalously frequent MJO phases 1 and 6 mask the extratropical teleconnection. An alternative interpretation could be that the MJO somehow modulates $P_{\rm EA}$ to render it a less effective driver of NAD during nonuniform years, but the lack of significant correlation between PC_{M1} and $P_{\rm EA}$ (r=0.13, p=0.31) does not support this alternative interpretation. However, there are ENSO-like SST variations that can influence MJO phase (Dasgupta et al. 2021) and EAM convection (Wu and Wang 2002), and these SST patterns could modulate changes in the relative importance of these two drivers of NAD.

While we consider the EAM and MJO mechanisms as drivers of the NAD, these two mechanisms may not influence the NAD's two centers of action equally. A one-point correlation map for Z_{500} using the NAD's western center of action as the origin yields a pan-Pacific Rossby wave pattern very similar to the result from uniform MJO summers in Fig. 8a, whereas a one-point correlation map for Z_{500} using the NAD's eastern center of action as the origin yields a Rossby wave from the central tropical Pacific very similar to the nonuniform MJO pattern in Fig. 8b. We might therefore interpret the NAD as the superposition of two standing Rossby waves—one triggered by EAM convection in a pattern most apparent in uniform MJO summers and one triggered by anomalies in the seasonal phase distribution of the MJO most apparent in non-uniform MJO summers.

An emerging paradigm in climate change ecology is that local-scale processes are constrained by environmental drivers operating over broad geographic scales, but studying these cross-scale relationships presents a significant interdisciplinary challenge. Most ecological studies are restricted to local or regional scales, and as a result, the effects of climatic dipoles on ecological processes is largely unexplored. Our findings underscore the importance of global teleconnections in shaping climate dipoles in North America and the resulting ecological effects on bird movements and migrations. Given the known ecological connections between masting and boreal bird movements, it is likely that these global teleconnections are influencing multiple ecological and environmental processes. Climate variability can synchronize populations of bird and plant populations at local and regional scales, and uncovering the origins of the climate dipoles offers new avenues of exploration.

Acknowledgments. This work was supported by National Foundation Award 1926221 and 1926428. We acknowledge the University of Utah Center of High Performance Computing (CHPC) for computational resources and computer support services. We thank Project FeederWatch, the Cornell Lab of Ornithology for the bird data, and we thank Ivy Widick for the data curation as well. Comments from the editor and three anonymous reviewers helped to improve the manuscript.

Data availability statement. The FeederWatch bird count observations used in this project are available from the Cornell Lab of Ornithology (https://www.birds.cornell.edu/home). Reanalysis data sets including geopotential height, air temperature, and OLR are available from the European Centre for Medium Range Weather Forecasts (https://www.ecmwf.int/en/ forecasts/datasets/reanalysis-datasets/era5) and NOAA PSL's Twentieth Century Reanalysis (https://psl.noaa.gov/data/). Sea surface temperature is from the Hadley Centre Sea Ice and Sea Surface Temperature dataset at https://www.metoffice. gov.uk/hadobs/hadsst2/, and the precipitation data are available from the Global Precipitation Climatology Center at https://climatedataguide.ucar.edu/climate-data/gpcc-globalprecipitation-climatology-centre and the Global Precipitation Climatology Project monthly data at https://psl.noaa. gov/data/gridded/data.gpcp.html.

REFERENCES

- Alberto, F. J., and Coauthors, 2013: Potential for evolutionary responses to climate change–evidence from tree populations. Global Change Biol., 19, 1645–1661, https://doi.org/10.1111/gcb.12181.
- Alerstam, T., 1993: Bird Migration. Cambridge University Press, 420 pp.
- Barrett, B. S., 2019: Connections between the Madden–Julian oscillation and surface temperatures in winter 2018 over eastern North America. Atmos. Sci. Lett., 20, e869, https://doi.org/10.1002/asl.869.
- Bock, C. E., and L. W. Lepthien, 1976: Synchronous eruptions of boreal seed-eating birds. *Amer. Nat.*, 110, 559–571, https://doi. org/10.1086/283091.
- Bonter, D. N., and W. M. Hochachka, 2009: A citizen science approach to ornithological research: Twenty years of watching backyard birds. *Proc. Fourth Int. Partners in Flight Conf. Tundra to Tropics*, McAllen, TX, Partners in Flight, 453–458.
- Compo, G. P., and Coauthors, 2011: The Twentieth Century Reanalysis project. *Quart. J. Roy. Meteor. Soc.*, 137, 1–28, https://doi.org/10.1002/qj.776.
- Cui, J., L. Wang, T. Li, and B. Wu, 2020: Can reanalysis products with only surface variables assimilated capture Madden–Julian oscillation characteristics? *Int. J. Climatol.*, 40, 1279–1293, https://doi.org/10.1002/joc.6270.
- Dasgupta, P., M. Roxy, R. Chattopadhyay, C. Naidu, and A. Metya, 2021: Interannual variability of the frequency of MJO phases and its association with two types of ENSO. *Sci. Rep.*, **11**, 11541, https://doi.org/10.1038/s41598-021-91060-2.
- Davis, M. B., and R. G. Shaw, 2001: Range shifts and adaptive responses to quaternary climate change. *Science*, 292, 673–679, https://doi.org/10.1126/science.292.5517.673.
- Ding, Q., B. Wang, J. M. Wallace, and G. Branstator, 2011: Tropical-extratropical teleconnections in boreal summer: Observed interannual variability. *J. Climate*, 24, 1878–1896, https://doi.org/10.1175/2011JCLI3621.1.
- Enomoto, T., B. J. Hoskins, and Y. Matsuda, 2003: The formation mechanism of the Bonin high in August. *Quart. J. Roy. Meteor. Soc.*, **129**, 157–178, https://doi.org/10.1256/qj.01.211.
- Fuentes-Franco, R., T. Koenigk, D. Docquier, F. Graef, and K. Wyser, 2022: Exploring the influence of the North Pacific Rossby wave sources on the variability of summer atmospheric circulation and precipitation over the Northern Hemisphere.

- Climate Dyn., **59**, 2025–2039, https://doi.org/10.1007/s00382-022-06194-4
- Hannachi, A., I. T. Jolliffe, and D. B. Stephenson, 2007: Empirical orthogonal functions and related techniques in atmospheric science: A review. *Int. J. Climatol.*, 27, 1119–1152, https://doi. org/10.1002/joc.1499.
- Hersbach, H., and Coauthors, 2020: The ERA5 global reanalysis. *Quart. J. Roy. Meteor. Soc.*, **146**, 1999–2049, https://doi.org/10.1002/qj.3803.
- Huffman, G. J., and Coauthors, 1997: The Global Precipitation Climatology Project (GPCP) combined precipitation dataset. Bull. Amer. Meteor. Soc., 78, 5–20, https://doi.org/10.1175/ 1520-0477(1997)078<0005:TGPCPG>2.0.CO;2.
- Koenig, W. D., 2001: Synchrony and periodicity of eruptions by boreal birds. Condor, 103, 725–735, https://doi.org/10.1093/ condor/103.4.725.
- —, and J. M. Knops, 2001: Seed-crop size and eruptions of North American boreal seed-eating birds. J. Anim. Ecol., 70, 609–620, https://doi.org/10.1046/j.1365-2656.2001.00516.x.
- Kosaka, Y., and H. Nakamura, 2006: Structure and dynamics of the summertime Pacific–Japan teleconnection pattern. *Quart. J. Roy. Meteor. Soc.*, **132**, 2009–2030, https://doi.org/10.1256/qj. 05.204.
- —, and —, 2010: Mechanisms of meridional teleconnection observed between a summer monsoon system and a subtropical anticyclone. Part I: The Pacific–Japan pattern. *J. Climate*, 23, 5085–5108, https://doi.org/10.1175/2010JCLI3413.1.
- LaMontagne, J. M., I. S. Pearse, D. F. Greene, and W. D. Koenig, 2020: Mast seeding patterns are asynchronous at a continental scale. *Nat. Plants*, 6, 460–465, https://doi.org/10.1038/s41477-020-0647-x.
- Lau, K.-M., and H. Weng, 2002: Recurrent teleconnection patterns linking summertime precipitation variability over East Asia and North America. J. Meteor. Soc. Japan, 80, 1309–1324, https://doi.org/10.2151/jmsj.80.1309.
- Li, X., D. M. Holland, E. P. Gerber, and C. Yoo, 2015: Rossby waves mediate impacts of tropical oceans on west Antarctic atmospheric circulation in Austral winter. *J. Climate*, 28, 8151–8164, https://doi.org/10.1175/JCLI-D-15-0113.1.
- Lopez, H., S.-K. Lee, S. Dong, G. Goni, B. Kirtman, R. Atlas, and A. Kumar, 2019: East Asian monsoon as a modulator of U.S. Great Plains heat waves. *J. Geophys. Res. Atmos.*, 124, 6342–6358, https://doi.org/10.1029/2018JD030151.
- Matthews, A. J., 2000: Propagation mechanisms for the Madden-Julian oscillation. *Quart. J. Roy. Meteor. Soc.*, **126**, 2637–2651, https://doi.org/10.1002/qj.49712656902.
- Moran, P. A. P., 1949: The statistical analysis of the sunspot and lynx cycles. J. Anim. Ecol., 18 115–116, https://doi.org/10. 2307/1585.
- Newton, I., 2012: Obligate and facultative migration in birds: Ecological aspects. J. Ornithol., 153, 171–180, https://doi.org/10.1007/s10336-011-0765-3.
- Nie, Y., Y. Zhang, X.-Q. Yang, and H.-L. Ren, 2019: Winter and summer Rossby wave sources in the CMIP5 models. *Earth Space Sci.*, 6, 1831–1846, https://doi.org/10.1029/2019EA000674.
- Nitta, T., 1987: Convective activities in the tropical western Pacific and their impact on the Northern Hemisphere summer circulation. J. Meteor. Soc. Japan, 65, 373–390, https://doi.org/10. 2151/jmsj1965.65.3_373.
- Princé, K., and B. Zuckerberg, 2015: Climate change in our backyards: The reshuffling of North America's winter bird communities. Global Change Biol., 21, 572–585, https://doi.org/10. 1111/gcb.12740.

- Sampe, T., and S.-P. Xie, 2010: Large-scale dynamics of the meiyubaiu rainband: Environmental forcing by the westerly jet. *J. Climate*, **23**, 113–134, https://doi.org/10.1175/2009JCLI3128.1.
- Sardeshmukh, P. D., and B. J. Hoskins, 1988: The generation of global rotational flow by steady idealized tropical divergence. *J. Atmos. Sci.*, 45, 1228–1251, https://doi.org/10.1175/1520-0469(1988)045<1228:TGOGRF>2.0.CO;2.
- Savolainen, O., T. Pyhäjärvi, and T. Knürr, 2007: Gene flow and local adaptation in trees. Annu. Rev. Ecol. Evol. Syst., 38, 595– 619, https://doi.org/10.1146/annurev.ecolsys.38.091206.095646.
- Scaife, A. A., and Coauthors, 2017: Tropical rainfall, Rossby waves and regional winter climate predictions. *Quart. J. Roy. Meteor. Soc.*, 143, 1–11, https://doi.org/10.1002/qj.2910.
- Schneider, U., T. Fuchs, A. Meyer-Christoffer, and B. Rudolf, 2008: Global precipitation analysis products of the GPCC. DWD Global Precipitation Climatology Centre, 112 pp.
- Sillett, T. S., R. T. Holmes, and T. W. Sherry, 2000: Impacts of a global climate cycle on population dynamics of a migratory songbird. *Science*, 288, 2040–2042, https://doi.org/10.1126/ science.288.5473.2040.
- Sokolov, L. V., M. Y. Markovets, V. Yefremov, and A. Shapoval, 2002: Irregular migrations (irruptions) in six bird species on the Courish Spit on the Baltic Sea in 1957–2002. Avian Ecol. Behav., 9, 39–53.
- Strong, C., B. Zuckerberg, J. L. Betancourt, and W. D. Koenig, 2015: Climatic dipoles drive two principal modes of North American boreal bird irruption. *Proc. Natl. Acad. Sci. USA*, 112, E2795–E2802, https://doi.org/10.1073/pnas.1418414112.
- Titchner, H. A., and N. A. Rayner, 2014: The Met Office Hadley Centre sea ice and sea surface temperature data set, version 2: 1. Sea ice concentrations. *J. Geophys. Res. Atmos.*, 119, 2864–2889, https://doi.org/10.1002/2013JD020316.
- Tseng, K.-C., E. Maloney, and E. Barnes, 2019: The consistency of MJO teleconnection patterns: An explanation using linear Rossby wave theory. *J. Climate*, 32, 531–548, https://doi.org/ 10.1175/JCLI-D-18-0211.1.
- Ventrice, M. J., M. C. Wheeler, H. H. Hendon, C. J. Schreck, C. D. Thorncroft, and G. N. Kiladis, 2013: A modified multivariate Madden–Julian oscillation index using velocity potential. *Mon. Wea. Rev.*, **141**, 4197–4210, https://doi.org/10.1175/ MWR-D-12-00327.1.
- Visser, M. E., A. C. Perdeck, J. H. Van Balen, and C. Both, 2009: Climate change leads to decreasing bird migration distances. *Global Change Biol.*, **15**, 1859–1865, https://doi.org/10.1111/j. 1365-2486.2009.01865.x.

- Wang, B., R. Wu, and K.-M. Lau, 2001: Interannual variability of the Asian summer monsoon: Contrasts between the Indian and the western North Pacific–East Asian monsoons. *J. Climate*, **14**, 4073–4090, https://doi.org/10.1175/1520-0442(2001)014<4073:IVOTAS>2.0.CO;2.
- Wang, Z., T. Li, and Y. Sun, 2021: Interdecadal variability of intensity of the Madden–Julian oscillation. *Atmos. Sci. Lett.*, 22, e1027, https://doi.org/10.1002/asl.1027.
- Watts, H. E., A. R. Robart, J. K. Chopra, C. E. Asinas, T. P. Hahn, and M. Ramenofsky, 2017: Seasonal expression of migratory behavior in a facultative migrant, the pine siskin. *Behav. Ecol. Sociobiol.*, 71, 9, https://doi.org/10.1007/s00265-016-2248-2.
- Wheeler, M. C., and H. H. Hendon, 2004: An all-season real-time multivariate MJO index: Development of an index for monitoring and prediction. *Mon. Wea. Rev.*, 132, 1917–1932, https://doi. org/10.1175/1520-0493(2004)132<1917:AARMMI>2.0.CO;2.
- Wu, R., and B. Wang, 2002: A contrast of the East Asian summer monsoon–ENSO relationship between 1962–77 and 1978–93. J. Climate, 15, 3266–3279, https://doi.org/10.1175/1520-0442(2002)015<3266:ACOTEA>2.0.CO;2.
- Zhang, C., 2005: Madden-Julian oscillation. Rev. Geophys., 43, RG2003, https://doi.org/10.1029/2004RG000158.
- Zhu, Z., and T. Li, 2016: A new paradigm for continental U.S. summer rainfall variability: Asia–North America teleconnection. J. Climate, 29, 7313–7327, https://doi.org/10.1175/JCLI-D-16-0137.1.
- —, and —, 2018: Amplified contiguous United States summer rainfall variability induced by East Asian monsoon interdecadal change. *Climate Dyn.*, **50**, 3523–3536, https://doi.org/10. 1007/s00382-017-3821-8.
- Zuckerberg, B., D. N. Bonter, W. M. Hochachka, W. D. Koenig, A. T. DeGaetano, and J. L. Dickinson, 2011: Climatic constraints on wintering bird distributions are modified by urbanization and weather. *J. Anim. Ecol.*, 80, 403–413, https://doi. org/10.1111/j.1365-2656.2010.01780.x.
- —, A. Desrochers, W. M. Hochachka, D. Fink, W. D. Koenig, and J. L. Dickinson, 2012: Overlapping landscapes: A persistent, but misdirected concern when collecting and analyzing ecological data. *J. Wildland Manage.*, 76, 1072–1080, https://doi.org/10.1002/jwmg.326.
- —, C. Strong, J. M. LaMontagne, S. S. George, J. L. Betan-court, and W. D. Koenig, 2020: Climate dipoles as continental drivers of plant and animal populations. *Trends Ecol. Evol.*, 35, 440–453, https://doi.org/10.1016/j.tree.2020.01.010.